Yavartanoo *et al. Int J Concr Struct Mater* (2025) 19:48
https://doi.org/10.1186/s40069-025-00792-2

International Journal of Concrete
Structures and Materials

RESEARCH **Open Access**

Cost-Effective Retrofitting Method for Dry-Stack Masonry Walls Using Fiber-Reinforced Polymers

Fahimeh Yavartanoo[1], Chang-Soo Kim[1*] and Thomas H.-K. Kang[2]

Abstract

Using fiber-reinforced polymer (FRP) has gained widespread acceptance as an effective method for strengthening masonry walls in seismic zones. This research focuses on analyzing the in-plane behavior of dry-stack masonry walls reinforced with embedded FRP bars, providing a cost-efficient solution. Three reinforcement layouts, including horizontal, vertical, and diagonal, each with varying numbers of bars, were investigated. Alongside various FRP materials such as carbon, aramid, and glass fibers, the study also encompasses titanium and stainless steel bars to ensure a comprehensive assessment. Two-dimensional nonlinear finite element models were proposed using ABAQUS software, employing a micro-modeling strategy to investigate the performance of retrofitted walls. The modeling approach was validated by comparing it with existing experimental data. The lateral response of the walls under vertical loads was evaluated using pushover and cyclic analysis methods for different arrangements and materials of bars to find the most efficient model. The findings indicated that vertically aligned S-Glass FRP outperforms other models in enhancing wall overstrength, stiffness hardening, and energy dissipation capacity.

Keywords Masonry structures, Retrofitting method, Stainless steel, Titanium, FRP, Pushover, Cyclic

1 Introduction

Masonry, traditional building material, has been widely utilized in construction for centuries. It remains a predominant form of construction, especially in rural and developing regions (Bhattacharya et al., 2014). Reinforced, unreinforced (plain), and confined masonry (Zamani Ahari, 2013) structures make up over 70% of the world's building inventory, reflecting their applicability and longevity (Wang et al., 2018). Unreinforced masonry (URM) structures, when constructed without adhering to appropriate design principles, perform inadequately under seismic loads, strong winds, blasts, and other similar forces (Sayin et al., 2019). The vulnerability of these non-engineered buildings makes them prone to brittle failure during seismic events. Lateral loads cause considerable shear and tensile stresses in masonry buildings, resulting in cracks that can spread throughout the system and, over time, lead to irreversible damage. However, such structures usually possess enough compressive strength to behave acceptably under normal gravity loads. To mitigate these hazards and balance the economic, safety, and quality-of-life concerns, a detailed study of these buildings is crucial. Over the past decades, significant improvements in the seismic performance of masonry buildings have been gained by conducting post-seismic assessments, experimental research, and analytical research. As a result, various advanced methods have been introduced for retrofitting masonry buildings, primarily focusing on improving the building's performance. In other words, conventional methods can be upgraded

---

Journal information: ISSN 1976-0485 / eISSN 2234-1315.

*Correspondence:
Chang-Soo Kim
changsookim@seoultech.ac.kr
[1] Seoul National University of Science and Technology, 232 Gongneung-ro, Nowon-gu, Seoul 01811, Korea
[2] Seoul National University, 1 Gwanak-ro, Gwanak-gu, Seoul 08826, Korea

by modern techniques aimed at enhancing both the energy dissipation capacity and the ductility of the structure (Paganoni & D'Ayala, 2015).

The fundamental principles of strengthening and retrofitting include: (i) improving structural integrity; (ii) reducing seismic demands; and (iii) increasing the load-carrying capacity of individual building components (Yavartanoo & Kang, 2022a). The effectiveness of these methodologies may differ depending on factors such as the material properties and the direction of the loads applied. Therefore, it is recommended to conduct both experimental and numerical investigations before implementing any specific method. The application of reinforcement bars, as a type of strengthening measure, has been used successfully in various structures over the years. Steel reinforcement, in particular, enhances ductility, seismic performance, in-plane strength, and the energy dissipation potential of the structure (Shrestha et al., 2011). This method significantly improves the structural performance of masonry walls, and load-bearing capacity can be further increased by utilizing high-strength steel elements. In recent years, fiber-reinforced polymer (FRP) composites have gained recognition as a promising material for retrofitting and strengthening masonry buildings. These materials offer significant improvements in both ductility and load-bearing capacity. Considerable research has been conducted on the use of FRP materials for retrofitting masonry structures, as documented in the available literature (Abdulsalam et al., 2021; Jing et al., 2023; Torres et al., 2022).

Dry-stack walls have been widely used in ancient construction as the main load-bearing system. Besides, many walls with mortar joints in old construction exhibit poor condition because of weathering and deterioration. For these cases, the strength of mortar can be neglected for conservatism, and they can be considered dry-stack type. These walls are more vulnerable to seismic loads than walls with mortar joints, and more investigations are required to understand and improve their behavior with practical methods.

This research seeks to simulate the mechanical response of dry-stack masonry walls reinforced with bars arranged in various configurations and materials, such as stainless steel, titanium, and FRP. The wall behavior is modeled through a nonlinear finite element approach, utilizing micro-modeling techniques. Initially, the validation of the nonlinear numerical model is conducted for an unreinforced masonry (URM) dry-stack wall, serving as the base model. This validation process involves comparing the failure mechanism and load–displacement response obtained from the model with previous experimental results (Vasconcelos, 2005). Afterward, different materials and configurations of bars are introduced into the base model for retrofitting, and the performance of the retrofitted wall is compared to the original. This comparison seeks to determine the most effective configuration in terms of performance under both monotonic and cyclic loads.

2 Retrofitting Strategy

The retrofitting procedure evaluates the performance of dry-stack masonry walls reinforced with embedded bars of various configurations and materials, tested under differing levels of vertical load. The bars were inserted laterally into the wall and secured to the support or side elements by embedding their ends or using appropriate anchorage devices installed at the top and sides of the wall. The required embedment length can be determined either through theoretical calculations or experimental validation (Yavartanoo et al., 2020). This technique requires no surface preparation and offers significantly reduced installation time compared to alternative methods. Embedding bars in three orientations of horizontal, vertical, and diagonal was considered, encompassing nine models of the most effective arrangements for each direction. Embedding diagonal bars into masonry walls presents significant challenges, and the near-surface mounted (NSM) method is more commonly employed for such arrangements (Askar et al., 2022; Jafari et al., 2018; Soleymani et al., 2023). Nonetheless, for the sake of comprehensiveness, the inclusion of diagonal bars in the numerical models was carried out in this study. Finite element models were evaluated by varying the number and positioning of bars, as well as the wall height, as depicted in Fig. 1. The labels, bar quantities, and specified spacing values for each type of arrangement are presented in Table 1. Each model was given a specific designation according to the number of bars, as illustrated in the table. For example, the HR1-2 model refers to horizontal arrangement type 1, which uses two bars.

Exploring high-quality materials with diverse geometries for reinforcement bars is an advancing area in modern engineering. Numerous materials are available for manufacturing reinforcement, each selected based on attributes such as availability, durability, and cost-effectiveness. Stainless steel, a type of iron-based alloy, excels in corrosion resistance while maintaining high strength at elevated temperatures. Titanium, though it has lower elastic stiffness than mild steel and stainless steel, offers similar or even greater yield strength (350–1200 MPa) with less density, high thermal conductivity, and exceptional corrosion resistance (Golden et al., 1952; Vintzileou & Papadopoulos, 2001). Composites, made of two or more distinct materials, are often preferred for use as structural reinforcement due to their superior properties and broad availability. Fiber-reinforced polymer

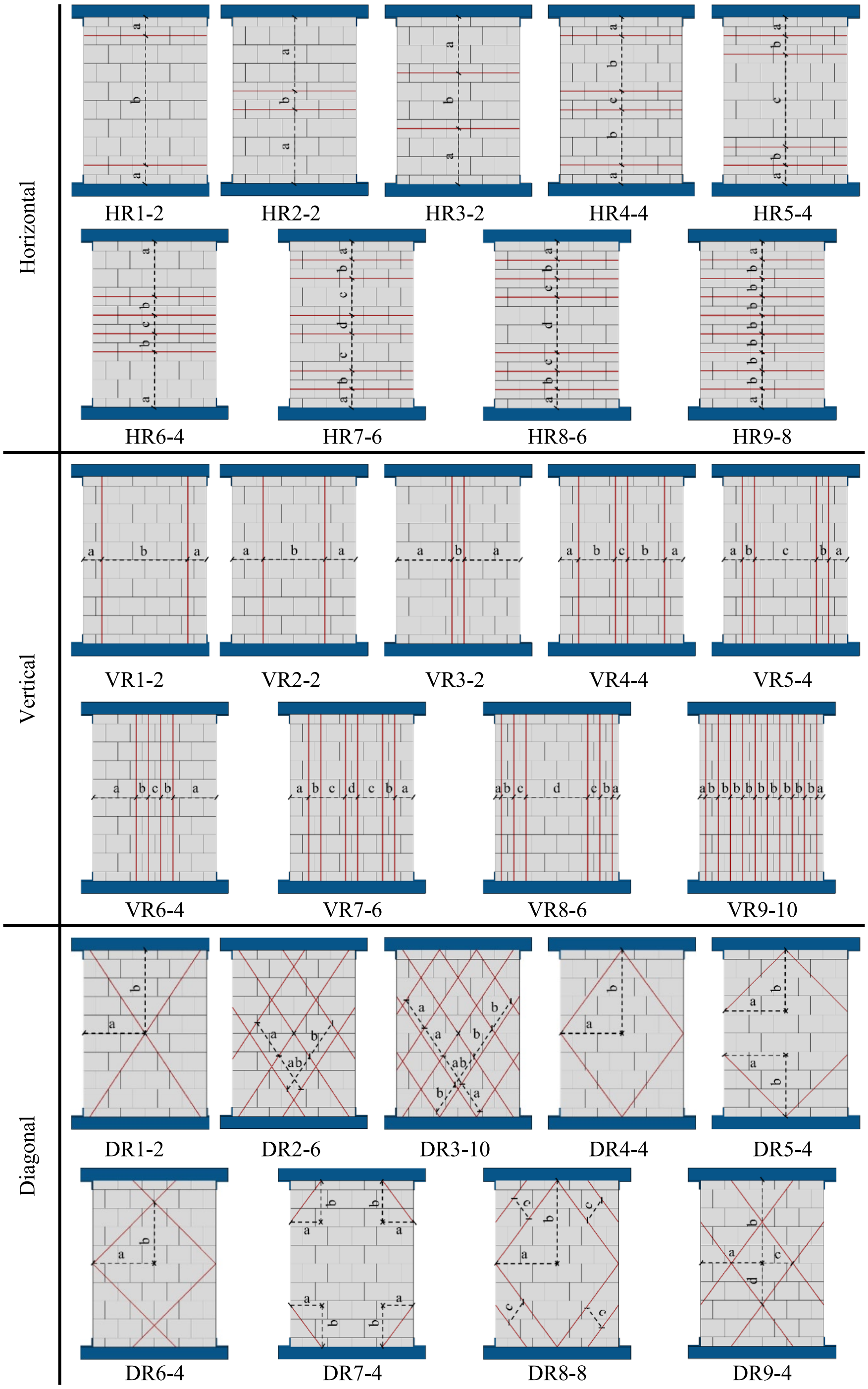

Fig. 1 Bars arrangements in the URM wall

(FRP) stands out for its lightweight nature, high tensile strength, and resistance to corrosion and magnetic forces. FRP materials are available in various forms, such as strips, sheets, and bars, having materials like aramid, glass, and carbon. As noted by ElGawady et al. (ElGawady et al., 2004), retrofitting walls with FRP enhances in-plane and out-of-plane resistance by factors of 1.1 to 3 and 7, respectively. FRP generally improves lateral resistance, load-bearing capacity, ductility, and energy absorption of retrofitted walls. Moreover, its gradual failure pattern helps prevent sudden failure in unreinforced masonry (URM) walls (Bhattacharya et al., 2014).

Table 1 Details of arrangement and number of bars

Type	Model	No. of bars	Space (mm)			
			a	*b*	*c*	*d*
Horizontal	HR1-2	2	150	1050	–	–
	HR2-2	2	600	150	–	–
	HR3-2	2	450	450	–	–
	HR4-4	4	150	450	150	–
	HR5-4	4	150	150	750	–
	HR6-4	4	450	150	150	–
	HR7-6	6	150	150	300	150
	HR8-6	6	150	150	150	450
	HR9-8	8	150	150	–	–
Vertical	VR1-2	2	150	700	–	–
	VR2-2	2	250	500	–	–
	VR3-2	2	450	100	–	–
	VR4-4	4	150	300	100	–
	VR5-4	4	150	100	500	–
	VR6-4	4	350	100	100	–
	VR7-6	6	150	100	150	100
	VR8-6	6	150	100	100	300
	VR9-10	10	50	100	–	–
Diagonal	DR1-2	2	500	675	–	–
	DR2-6	6	300	300	–	–
	DR3-10	10	250	250	–	–
	DR4-4	4	500	675	–	–
	DR5-4	4	500	500	–	–
	DR6-4	4	500	500	–	–
	DR7-4	4	250	350	–	–
	DR8-8	8	500	675	200	–
	DR9-4	4	500	675	250	337.5

Although installation costs and technological requirements are relatively high, the minimal added mass, low disturbance, and substantial strength improvements make FRP an ideal choice for rehabilitation. Additional studies on the advantages and limitations of FRP as a retrofit material for masonry buildings can be found in the literature (Bui et al., 2015; Capozucca, 2011; Noor-E-Khuda et al., 2016; Saghafi et al., 2014; Turco et al., 2006).

FRP composites are commonly made from carbon, aramid, or glass fibers. Carbon fiber-reinforced polymers (CFRP) are available in two forms depending on requirements: high-modulus and high-strength polymers. In this study, these types are labeled CFRP1 and CFRP2. Glass fiber-reinforced polymers (GFRP) typically fall into two categories: electrical-glass (E-glass), known for its low electrical conductivity, and strength-glass (S-glass), recognized for its high tensile strength (Islam, 2008), and they are designated as EGFRP and SGFRP, respectively, in this study. The aramid-based fiber-reinforced polymer is referred to as AFRP in this research.

FRP materials possess greater strength than both titanium and stainless steel. They demonstrate linear elastic behavior until reaching their ultimate strength, at which point they tend to fail abruptly due to their brittle characteristics. In contrast, titanium and stainless steel exhibit considerable ductility prior to failure.

This research examines the behavior of URM walls retrofitted with stainless steel (SS), titanium (Ti), and five different types of FRP bars. The material properties investigated in previous experimental studies are detailed in Table 2 (Islam, 2008; Shrestha et al., 2011b; Yavartanoo et al., 2020). Additionally, a constant diameter (d) of 6 mm was used in all cases.

3 Numerical Modeling Assumptions

3.1 Verifying the Numerical Model

The experimental test results on dry-stack URM walls from the study by Vasconcelos (2005) were used as a

Table 2 Material properties of bars ($d = 6$ mm)

Material	Symbol	E (GPa)	F_u (MPa)
Stainless steel	SS	200	667
Titanium	Ti	70.6	363.4
FRP			
Carbon			
High-modulus	CFRP1	390–760	2400–3400
High-strength	CFRP2	240–280	4100–5100
Glass			
E-glass	EGFRP	70–80	2000–3500
S-glass	SGFRP	85–90	3500–4800
Aramid	AFRP	62–180	3600–3800

reference for validating the numerical model and assessing the URM wall performance (Fig. 2a). The URM dry-stack wall specimen has 1 m length, 1.35 m height, and 0.2 m width. The main part of the wall (clear span) includes eight layers of stone units, each with a height of 15 cm. Additionally, there is one extra layer at both the top and bottom of the wall, comprising stone units with a height of 7.5 cm each. These two additional layers are tightly connected to the rigid beams and further confined with angles on the left and right sides. The in-plane response of the specimen was evaluated under monotonic lateral loads, with four distinct levels of vertical load applied (σ): 0.2 MPa (40 kN), 0.5 MPa (100 kN), 0.875 MPa (175 kN), and 1.25 MPa (250 kN).

A nonlinear finite element (FE) model was constructed using the micro-modeling approach in a 2D plane-stress framework, employing ABAQUS software (Abaqus, 2020). Top and bottom beams and masonry units were discretized by the CPS4, which is a continuum plane-stress element with 4 nodes (linear shape function) and full integration points. Joint behavior was modeled using surface-to-surface contact (representing the line contact in the 2D model) with normal and tangential behavior. Normal contact behavior was modeled as hard contact under compressive stress, with separation permitted under tensile forces, assuming zero tensile strength. Tangential behavior was simulated using Coulomb's friction law, incorporating a friction coefficient ($\mu = 0.55$) and applying a penalty method for stiffness, based on Vasconcelos (2005) and Yavartanoo and Kang (2022). The FE model was calibrated and validated against experimental data, considering four levels of vertical load. Experimental tests revealed no signs of inelastic behavior within the masonry units. Therefore, for the scope of this study, masonry units were treated as a homogeneous material with isotropic elastic characteristics. This assumption simplified the model, requiring only the elastic modulus and Poisson's ratio as the primary material parameters. The material and mechanical properties of the masonry wall are reported in Table 3. Stiffness (K), yield strength (F_y), and ultimate strength (F_u) values listed in the table were derived from the load–displacement curves obtained from monotonic testing of specimens.

Fig. 2 depicts the load–displacement curves and failure mechanism for the calibrated model subjected to monotonic and cyclic loads and the vertical load of 1.25 MPa. In Fig. 2a, joint opening is depicted as the failure mechanism, accompanied by stress distribution within the stone units. Mises stress is utilized to represent multiaxial stress conditions in the stone units, which is an equivalent stress value commonly employed in nonlinear material models

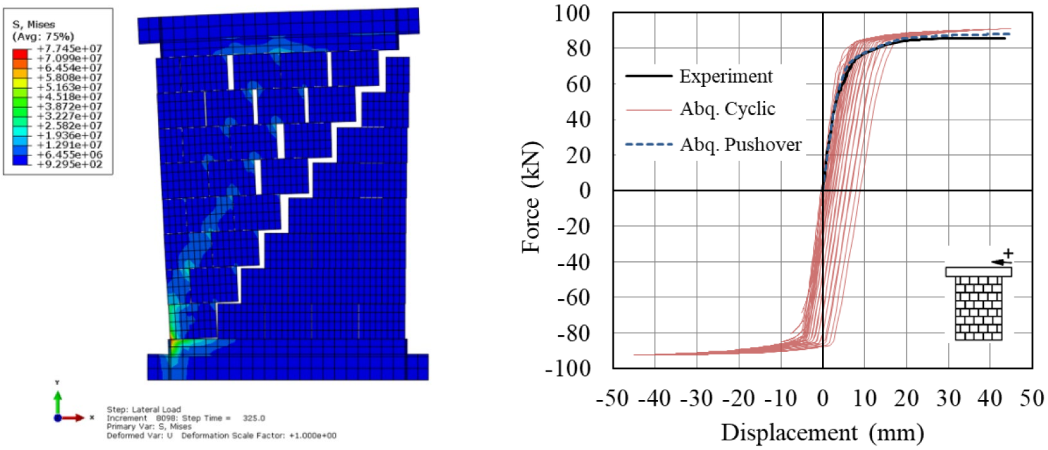

(a) Failure mechanism under cyclic load (d) load-displacement curves

Fig. 2 Response of calibrated FE model under monotonic and cyclic load ($\sigma = 1.25$ MPa). **a** Failure mechanism under cyclic load. **b** Load–displacement curves

Table 3 Mechanical properties of masonry walls

Parameter	Vertical load, σ (MPa)			
	0.2	**0.5**	**0.875**	**1.25**
Unit				
E (MPa)	2734.0	3287.5	4068.9	4722.0
Wall				
K (kN/mm)	8.81	9.89	15.54	16.65
F_y (kN)	10.81	26.73	48.24	66.09
F_u (kN)	16.13	36.94	63.17	85.83

to assess material yield or fracture. The load–displacement curve characteristics (stiffness and strength) and the failure mechanism (stair-stepped joint opening) from both the numerical model and experimental results closely align, supporting the model's validity. Additional information on the calibration and validation process of the numerical model is available in the study by Yavartanoo and Kang (2022).

In this study, the behavior of units is characterized by elastic material, which cannot explicitly consider material failure. Consequently, meticulous attention is warranted to verify the reliability of the outcomes through an assessment of stress distribution within the units. Notably, Vasconcelos (Vasconcelos, 2005) reported the absence of compressive crushing in any of the units during testing. According to numerical modeling results, the maximum Mises stress is about 77 MPa. Therefore, the actual strength of the material employed in the experiment should surpass this threshold, aligning with the typical compressive strength of granite stones, estimated to be around 100 MPa or higher (Huang & Lu, 2021; Ludovico-Marques et al., 2012; Vasconcelos, 2005; Vasconcelos et al., 2009; Yavartanoo et al., 2019). Based on these explanations, it was supposed that the compressive strength of the stone units is approximately 80 MPa.

The stress in all models has been carefully checked to ensure it does not exceed this value. This validation procedure implicitly confirms the accuracy of the results obtained by the models, considering the elastic behavior of the stone units.

3.2 Consideration for Modeling of Embedded Bars for Retrofitted Walls

To investigate the retrofitting method for dry-stack walls, finite element models were developed by incorporating bars into the calibrated model. As a result, key parameters such as material properties, joint behavior, methods of analysis, and boundary conditions were identical to those in the calibrated model. The bars were represented as line geometry and discretized using the T2D2 element, a type of truss element with two nodes (linear shape function) in 2D space. In practical applications, the inserted bars are connected to the masonry units using suitable adhesive materials, such as epoxy resin or cement-based grout. The bond's behavior depends on the properties of the bars, masonry, and adhesive materials, as well as the strength of the interfaces between masonry-adhesive and bar-adhesive. This study assumes that the adhesive material, along with the masonry-adhesive and bar-adhesive interfaces, has greater strength than the bars and masonry themselves. Thus, the bond behavior is primarily governed by the properties of the bars and masonry, with other potential failure modes being disregarded. Also, the bars are properly and tightly anchored at their ends. In this way, bars were positioned within the masonry employing the "Embedded region" constraint, which is identical to the no-slip condition between the bars and the masonry units.

Titanium and stainless steel were modeled with linear elastic–perfect plastic behavior. For FRP materials, an elastic–brittle model was applied, with linear elasticity up to the ultimate strength (F_u), followed by a linear softening plastic response until a reduced strength (F_r) is reached, simulating material rupture (Afzali et al., 2021). Although the material behavior is essentially linear, a small softening branch was introduced after F_u to avoid numerical instability associated with the sudden loss of capacity upon rupture. The software considers a perfect plastic behavior automatically for the strain larger than the corresponding strain at the defined reduced strength (ε_r). The slope of the linear softening plastic part was defined by F_u and its corresponding strain (ε_u), F_r, and ε_r. The values of F_r and ε_r were adjusted according to F_u and ε_u to realistically represent the damaged material realistically and prevent numerical instability. Therefore, a set of primary analyses have been performed for this issue. Based on the results, $F_r = 0.001F_y$ and $\varepsilon_r = \varepsilon_u + 0.001$ were used in the main analyses.

Given that stainless steel and titanium materials exhibit comparable coefficients of thermal expansion (CTE) to granite, there are no significant concerns regarding the behavior of retrofitted walls utilizing these materials. However, it is essential to note that FRP materials have anisotropic behavior, leading to varying thermal behaviors depending on the direction. Typically, in the longitudinal direction of FRP bars, parallel to the fibers, the CTE is minimal, sometimes even negative. Conversely, in the transverse direction, where the behavior is governed by the resin, the CTE can be considerably larger, ranging from 3 to 6 times that of concrete and granite (Galati et al., 2006; Gentry & Hudak, 1996). This discrepancy could adversely impact the bond behavior between FRP bars and granite stone units. While this study did not directly investigate this issue, it is imperative to recognize its significance and the need for further exploration with a focus on precisely evaluating the effect of temperature variations on bond behavior. It is worth emphasizing that in this study, it is assumed that the bars are adequately anchored at the ends. Consequently, even if there were partial bond interface failures due to differential thermal expansion between FRP and granite, the bars would still be able to effectively resist loads, thereby minimizing the potential impact on overall load-bearing capacity.

4 Results and Discussion

In the upcoming sections, the results of pushover analysis for different arrangements and materials will first be discussed. Subsequently, the response will be compared to identify the optimum arrangement and material, and finally, the results of cyclic analysis will be detailed.

4.1 Pushover Analysis

4.1.1 Stainless Steel and Titanium Bars

The results for dry-stack walls retrofitted with horizontal bars (Fig. 3a) show minimal improvement in the proposed configurations. While a marginal increase in wall strength is observed under the lowest vertical load ($\sigma = 0.2$ MPa), the impact significantly diminishes under higher vertical loads. This is due to the fact that horizontal bars do not enhance the tensile strength at horizontal joints, which typically open under lateral loading. The failure mode in walls retrofitted with horizontal bars involved both horizontal sliding and flexural (rocking) failure, except for the HR1-2 model, which exhibited a stair-stepped failure mode. However, horizontal sliding failure contributed less under higher vertical loads due to increased (frictional) shear strength. As horizontal bars increase tensile strength in vertical joints, flexural (rocking) failure was observed rather than stair-stepped joint opening (Fig. 4a). Based on these results, the inclusion of horizontally arranged bars was deemed ineffective. The stress developed in the models in all cases (Fig. 4a) is approximately half the assumed strength, which confirms the accuracy of the results.

Fig. 3b displays the load–displacement curves for walls retrofitted with vertical stainless steel bars under the maximum vertical load. All nine configurations led to notable hardening and overstrength in the system. While the non-retrofitted wall displayed elastic-perfect plastic behavior, the retrofitted walls showed elastic-hardening plastic behavior with considerable ductility.

Despite similar trends in the load–displacement curves across varying vertical loads, two key differences emerged. As the vertical load increases, the additional overstrength diminishes relative to the original strength. A softening phase follows the peak strength at lower vertical loads, except in the VR1-2, VR2-2, and VR3-2 models. With higher vertical loads, the softening phase transitions into perfectly plastic behavior. The results indicated that the VR3-2, VR6-4, and VR7-6 models were the most efficient and practical among the proposed configurations. Fig. 4b illustrates the failure mechanisms of these walls at a target displacement of 45 mm under the maximum vertical load. Both VR3-2 and VR6-4 exhibited stair-stepped failure mechanisms, but while VR3-2's crack pattern resembled that of the original wall, VR6-4 developed cracks at mid-height on the side rather than at the top-right corner. In contrast, the VR7-6 model primarily experienced flexural failure, with joints opening along the baseline rather than in a stair-stepped pattern. A similar observation was obtained for the walls retrofitted with vertical titanium bars. The stress generated in the models across all cases (Fig. 4b) is approximately half of the assumed strength, validating the accuracy of the results. Table 4 presents the ratios of ultimate strength between the retrofitted walls (F_{uR}) and the original walls (F_{uURM}) for models incorporating vertical stainless steel and titanium bars. Across all levels of vertical loads, the VR7-6 model exhibited the highest strength. However, the strength ratio decreased with higher vertical loads.

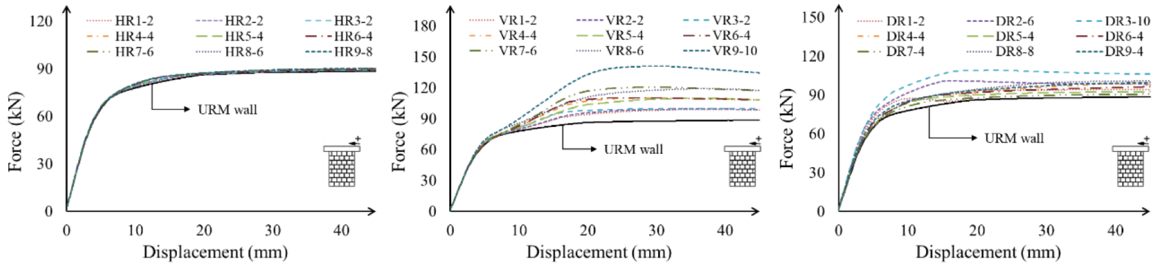

(a) horizontal (b) vertical (c) Diagonal

Fig. 3 The load–displacement curves of walls retrofitted with SS bars ($\sigma = 1.25$ MPa). **a** Horizontal, **b** Vertical, **c** Diagonal

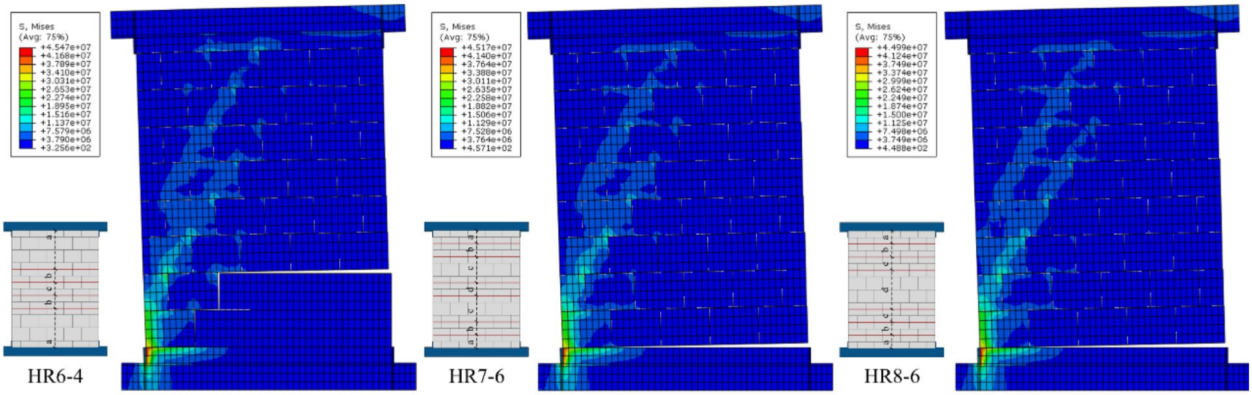

(a) Horizontal arrangement

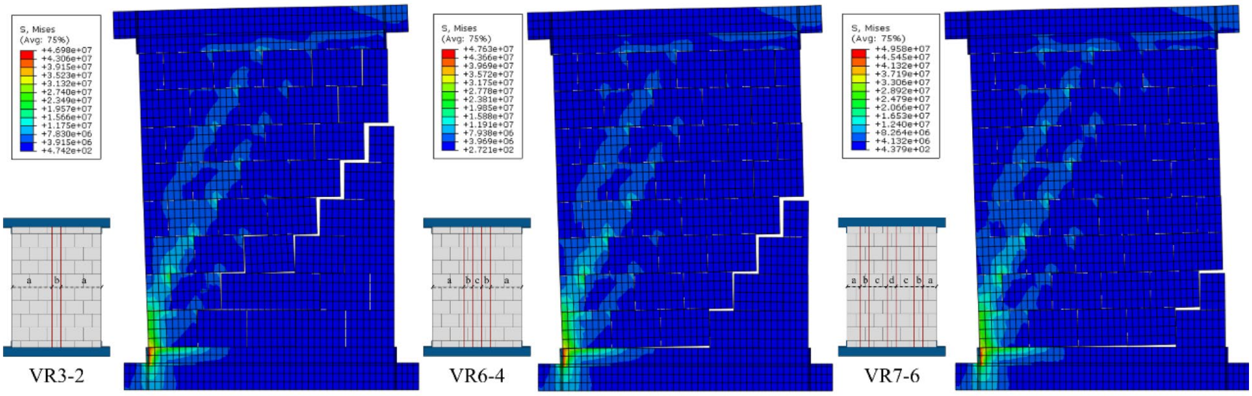

(b) Vertical arrangement

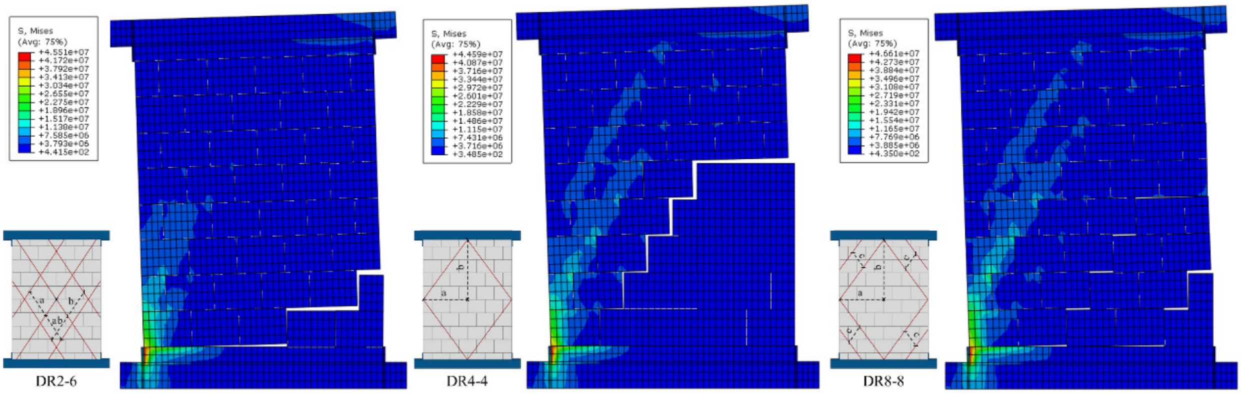

(c) Diagonal arrangement

Fig. 4 The failure mechanism of walls retrofitted with SS bars ($\sigma = 1.25$ MPa). **a** Horizontal arrangement. **b** Vertical arrangement. **c** Diagonal arrangement

For the third configuration, bars were positioned diagonally within the masonry wall at varying lengths and positions. Fig. 3c illustrates the load–displacement curves for walls strengthened with diagonal stainless steel bars. The load–displacement curves for the DR5-4 and DR7-4 models exhibit the lowest performance in terms of overstrength and hardening stiffness. Conversely, the DR2-6 and DR3-10 models displayed the highest levels of overstrength and hardening stiffness. Under lower vertical loads, these models exhibited significant softening upon reaching peak strength. As the vertical load increased, the softening phase lessened, transitioning

Table 4 The strength wall retrofitted with vertical SS and Ti bars (F_{uR}/F_{uURM})

σ (MPa)	**Material**	**Type**					
		VR3-2	**VR6-4**	**VR7-6**	**DR2-6**	**DR4-4**	**DR8-8**
0.2	SS	1.79	2.57	3.24	2.10	1.65	1.76
	Ti	1.42	1.87	2.27	1.62	1.37	1.43
0.5	SS	1.32	1.64	1.93	1.41	1.27	1.32
	Ti	1.17	1.35	1.53	1.22	1.15	1.18
0.875	SS	1.18	1.36	1.53	1.22	1.16	1.19
	Ti	1.10	1.20	1.30	1.12	1.09	1.11
1.25	SS	1.13	1.25	1.36	1.14	1.11	1.14
	Ti	1.07	1.14	1.20	1.08	1.06	1.08

into perfect plastic behavior. The load–displacement curves for the other models are fairly consistent, with DR4-4 and DR8-8 achieving the highest overstrength and hardening stiffness. According to the results, the DR2-6, DR4-4, and DR8-8 models were recognized as the most effective and practical solutions among the proposed configurations. Fig. 4c illustrates the failure mechanisms of the walls at a target displacement of 45 mm and a vertical load of 1.25 MPa.

Both the DR4-4 and VR8-8 models exhibited comparable failure mechanisms, characterized by stair-stepped cracking under low vertical loads. However, the bars restricted joint opening compared to the original walls. As the vertical load increased, the stair-stepped crack evolved into a flexural (horizontal) form at mid-height on the side, followed by further stair-stepped cracking initiating at the middle of the width. In contrast, the DR2-6 model predominantly experienced flexural failure, with joints opening along the baseline instead of exhibiting a stair-stepped pattern. A similar pattern was observed in the walls retrofitted with diagonal titanium bars. The stresses developed in all models, as illustrated in Fig. 4c, were almost half the assumed strength, confirming the reliability of the results.

Table 4 highlights the ratios of ultimate strength between the retrofitted walls (F_{uR}) and the original walls (F_{uURM}) for models incorporating stainless steel and titanium diagonal bars. The DR8-8 and DR2-6 models exhibited higher strength across all vertical load levels, although the strength ratio declined under higher vertical loads.

4.1.2 FFRP Bars

Fig. 5 illustrates the load–displacement curves of walls retrofitted with vertical FRP bars under maximum vertical loads. A notable increase in hardening and overstrength was observed in the retrofitted walls, similar to the behavior seen in walls retrofitted with stainless steel and titanium bars.

The retrofitted walls display elastic-hardening plastic behavior with considerable ductility. Although the overstrength contributed by FRPs is substantially higher than that of stainless steel and titanium, the strength quickly drops to match the original wall's strength after achieving peak strength. This behavior is due to the brittle nature of FRP materials.

The yielding displacement, δ_y, for different FRP models remains nearly identical, with values of 1.7, 2.9, 4.3, and 5.3 mm under vertical loads of 0.2, 0.5, 0.875, and 1.25 MPa, respectively. The displacements at FRP failure, δ_u, were derived from the curve, and ductility, $(\delta_u—\delta_y)/\delta_y$, was calculated and presented in Table 5. Table 5

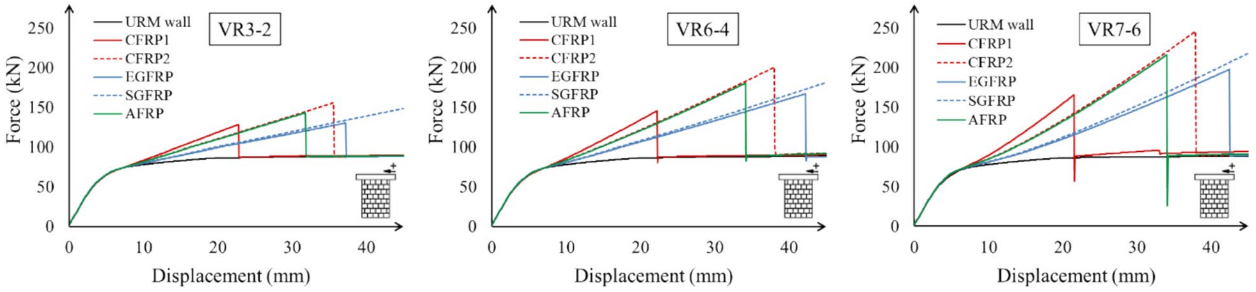

Fig. 5 The load–displacement curve of walls retrofitted with vertical FRP bars ($\sigma = 1.25$ MPa)

also includes the ratios of ultimate strength (F_{uR}/F_{uURM}), hardening stiffness (K_{hs}), and initial stiffness (K_{URM}) of the original wall, with K_{URM} adapted from the calibrated model. The ratio of F_{uR} to F_{uURM} serves as the overstrength factor for walls retrofitted with FRP bars.

Fig. 6a and b depicts the failure mechanisms of walls retrofitted with vertical bars using various types of FRP materials at the target displacement. In the VR7-6 model, the failure mechanism for all FRP materials involved flexural failure, with joints opening along the baseline, similar to what was observed with stainless steel and titanium materials. However, joint openings for EGFRP and SGFRP were smaller compared to other FRP materials, attributed to their higher ductility. For the VR6-4 models, the failure mechanism was primarily flexural failure in most cases. The stresses observed in all models (Fig. 6) were lower than the assumed strength, confirming the accuracy of the results.

Fig. 7 illustrates the load–displacement curves of walls retrofitted with diagonal bars using various FRP materials. In all cases, significant increases in hardening stiffness and overstrength were observed, similar to the behavior seen with stainless steel and titanium arrangements. In every case, as vertical load increases, the effect becomes more pronounced, and the retrofitted walls display elastic-hardening plastic behavior. Although FRPs provide greater overstrength compared to stainless steel and titanium, the strength quickly drops back to that of the original wall after reaching peak strength, due to the brittle nature of FRP materials.

Among the configurations considered, the DR2-6 model demonstrated the greatest overstrength and hardening stiffness but exhibited the least ductility. The DR4-4 and DR8-8 models showed similar performance in terms of overstrength and hardening stiffness, although DR8-8 exhibited higher ductility, the greatest of the three. According to the force–displacement curves, the yielding displacements, δ_y, for the different FRP models were nearly the same, with values of 2.1, 3.0, 4.5, and 6.2 mm under vertical loads of 0.2, 0.5, 0.875, and 1.25 MPa, respectively. The values of (K_{hs} /K_{URM}) and (F_{uR} /F_{uURM}) were computed similarly to the case with vertical bars and are presented in Table 5.

Across the three arrangement models (DR2-6, VR4-4, and VR8-8), CFRP2 and SGFRP delivered the highest overstrength, with similar values ranging from 1.35 to 6.95 for CFRP2 and 1.37 to 6.53 for SGFRP at varying vertical load levels. CFRP2 showed greater hardening stiffness, ranging from 0.16 to 0.95 under different vertical loads, while SGFRP demonstrated higher ductility, varying between 2.16 and 20.43 depending on the vertical load. Thus, CFRP2 and SGFRP can be considered the most efficient options. Failure mechanisms of walls retrofitted by diagonal CFRP2 and SGFRP bars at the target displacement are shown in Fig. 8a and b.

Overall, the failure mechanisms closely resembled those seen in diagonal stainless steel and titanium bars. However, in most instances, the FRP bars reached their ultimate strength at a lower lateral displacement than the target value. Consequently, the failure mechanisms observed at the target displacements, as shown in the figures, were a mixture of the failure modes observed in stainless steel and titanium materials, with some localized sliding occurring near the fractured FRP bars. In situations where the FRP bars either remained intact or fractured close to the target displacements, minor localized sliding was noted, with failure modes similar to those of stainless steel and titanium. The stresses observed across all models (Fig. 8) were nearly half of the assumed strength, verifying the accuracy of the findings.

4.2 Comparative Studies Based on Pushover Analysis

The findings suggest that horizontal bar arrangements have minimal influence on the seismic behavior of the wall. In contrast, vertical and diagonal bars significantly enhance the seismic performance by providing substantial overstrength and hardening stiffness. Among the examined configurations, the VR3-2, VR6-4, and VR7-6 vertical models, along with the DR2-6, DR4-4, and DR8-8 diagonal models, showed superior performance compared to the other cases. Results from the FRP bar models reveal that CFRP2 offers greater strength compared to other FRP types, while SGFRP provides more ductility with nearly the same strength as CFRP2. Therefore, CFRP2 and SGFRP, as well as stainless steel and titanium, were selected for comparative studies. The outcomes of these models were compared to identify the most efficient retrofit case in terms of material and configuration, as shown in Fig. 9a and b. It is evident that VR7-6 models have the highest efficiency regarding overstrength and hardening stiffness under both lower and upper levels of vertical load. While both stainless steel and titanium bars offer high ductility, stainless steel produces greater overstrength and a steeper hardening slope than titanium. CFRP2 and SGFRP, however, deliver much higher overstrength and hardening stiffness compared to stainless steel across both lower and upper vertical loads. Although CFRP2 offers greater overstrength and hardening stiffness than SGFRP, it failed to maintain the target displacement and was interrupted. Conversely, SGFRP did not achieve ultimate strength at the target displacements. Thus, the combination of SGFRP with the VR7-6 configuration can be regarded as the most effective vertical solution.

Similar to the vertical models, stainless steel and titanium bars exhibit significant ductility across all three

Table 5 Ductility, hardening stiffness, and strength of retrofitted walls with vertical and diagonal FRP bars under different vertical loads (σ)

Type	σ (MPa)	Ductility			K_{hs}/K_{URM}			F_{uR}/F_{uURM}		
		VR3-2	**VR6-4**	**VR7-6**	**VR3-2**	**VR6-4**	**VR7-6**	**VR3-2**	**VR6-4**	**VR7-6**
CFRP1	0.2	11.74	12.26	12.00	0.36	0.51	0.70	3.81	5.30	6.86
	0.5	6.56	6.77	6.51	0.26	0.36	0.48	2.17	2.79	3.39
	0.875	4.18	4.18	4.01	0.23	0.31	0.44	1.66	1.99	2.32
	1.25	3.31	3.20	3.07	0.22	0.29	0.37	1.45	1.64	1.87
		DR2-6	DR4-4	DR8-8	DR2-6	DR4-4	DR8-8	DR2-6	DR4-4	DR8-8
	0.2	3.21	5.96	6.07	1.26	0.32	0.33	4.45	2.58	2.61
	0.5	1.83	3.48	3.55	0.91	0.23	0.23	2.28	1.53	1.54
	0.875	0.80	1.73	1.88	1.02	0.25	0.12	1.61	1.22	1.23
	1.25	0.41	1.04	1.05	0.55	0.11	0.12	1.32	1.13	1.13
		VR3-2	VR6-4	VR7-6	VR3-2	VR6-4	VR7-6	VR3-2	VR6-4	VR7-6
CFRP2	0.2	20.96	22.26	22.13	0.31	0.46	0.64	5.42	8.18	11.08
	0.5	11.56	12.40	12.30	0.22	0.32	0.44	2.88	4.10	5.32
	0.875	7.28	7.93	7.88	0.19	0.27	0.37	2.09	2.81	3.53
	1.25	5.74	6.21	6.20	0.18	0.25	0.34	1.76	2.27	2.78
		DR2-6	DR4-4	DR8-8	DR2-6	DR4-4	DR8-8	DR2-6	DR4-4	DR8-8
	0.2	7.21	13.25	13.93	0.95	0.26	0.26	6.95	3.88	4.09
	0.5	4.43	8.10	8.58	0.67	0.18	0.18	3.41	2.08	2.17
	0.875	2.33	4.58	4.80	0.64	0.17	0.17	2.29	1.55	1.60
	1.25	1.37	2.97	3.09	0.66	0.16	0.16	1.83	1.35	1.37
		VR3-2	VR6-4	VR7-6	VR3-2	VR6-4	VR7-6	VR3-2	VR6-4	VR7-6
EGFRP	0.2	21.96	23.61	23.52	0.19	0.30	0.41	3.77	5.84	7.71
	0.5	12.08	13.40	13.40	0.14	0.21	0.28	2.17	3.09	3.90
	0.875	7.55	8.77	8.77	0.13	0.18	0.24	1.68	2.25	2.72
	1.25	6.07	7.04	7.06	0.12	0.17	0.22	1.47	1.89	2.23
		DR2-6	DR4-4	DR8-8	DR2-6	DR4-4	DR8-8	DR2-6	DR4-4	DR8-8
	0.2	6.21	14.43	16.04	0.66	0.15	0.16	4.65	2.77	3.10
	0.5	3.90	8.80	10.00	0.47	0.11	0.11	2.47	1.65	1.81
	0.875	2.17	5.13	5.80	0.45	0.11	0.04	1.77	1.33	1.41
	1.25	1.36	3.59	3.87	0.45	0.05	0.10	1.51	1.22	1.26
		VR3-2	VR6-4	VR7-6	VR3-2	VR6-4	VR7-6	VR3-2	VR6-4	VR7-6
SGFRP	0.2	25.09	25.09	25.09	0.21	0.32	0.44	4.51	6.57	8.81
	0.5	14.38	14.30	14.30	0.15	0.22	0.30	2.55	3.44	4.41
	0.875	9.47	9.47	9.47	0.13	0.19	0.26	1.96	2.47	3.06
	1.25	7.57	7.57	7.57	0.13	0.18	0.24	1.68	2.05	2.46
		DR2-6	DR4-4	DR8-8	DR2-6	DR4-4	DR8-8	DR2-6	DR4-4	DR8-8
	0.2	9.57	20.32	20.43	0.67	0.16	0.17	6.53	3.79	3.94
	0.5	6.03	12.8	14.00	0.47	0.11	0.12	3.27	2.07	2.25
	0.875	3.40	7.47	8.60	0.43	0.10	0.11	2.25	1.56	1.70
	1.25	2.16	5.07	5.59	0.42	0.10	0.10	1.83	1.37	1.44
		VR3-2	VR6-4	VR7-6	VR3-2	VR6-4	VR7-6	VR3-2	VR6-4	VR7-6
AFRP	0.2	18.09	19.43	19.52	0.30	0.44	0.60	4.62	6.96	9.32
	0.5	10.00	10.90	10.90	0.21	0.30	0.41	2.54	3.56	4.54
	0.875	6.34	6.95	6.95	0.19	0.26	0.35	1.89	2.49	3.07
	1.25	5.03	5.47	5.46	0.18	0.24	0.32	1.62	2.04	2.44
		DR2-6	DR4-4	DR8-8	DR2-6	DR4-4	DR8-8	DR2-6	DR4-4	DR8-8
	0.2	5.75	10.82	11.43	0.96	0.25	0.25	5.75	3.25	3.43
	0.5	3.53	6.55	6.93	0.68	0.18	0.18	2.90	1.82	1.89
	0.875	1.80	3.68	3.85	0.67	0.17	0.17	1.98	1.41	1.44
	1.25	1.03	2.36	2.95	0.71	0.17	0.14	1.63	1.25	1.27

CFRP1: carbon fiber-reinforced polymer with high-modulus; CFRP2: carbon fiber-reinforced polymer with high-strength; EGFRP: electrical-glass fiber-reinforced polymer; SGFRP: strength-glass fiber-reinforced polymer; AFRP: aramid fiber-reinforced polymer

diagonal cases (Fig. 9c and d). Stainless steel provides greater overstrength and stiffness compared to titanium bars. Additionally, SGFRP and CFRP2 consistently deliver higher overstrength and stiffness than stainless steel. Of the three selected diagonal configurations, the DR2-6/CFRP2 model exhibited the highest overstrength and hardening stiffness, while the DR8-8/SGFRP model demonstrated the greatest ductility. Under

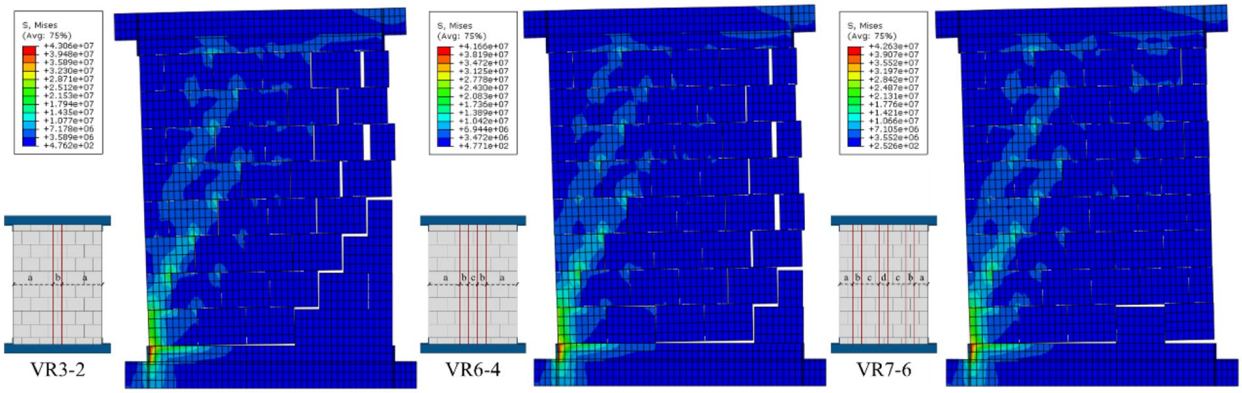

(a) Retrofitted with vertical CFRP2 bars

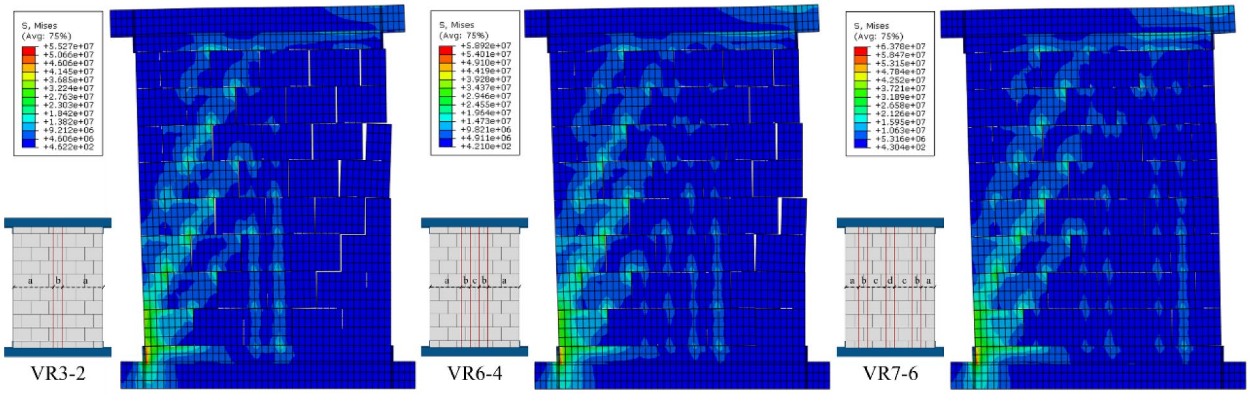

(b) Retrofitted with vertical SGFRP bars

Fig. 6 The failure mechanism of walls retrofitted with vertical CFRP2 and SGFRP bars ($\sigma = 1.25$ MPa). **a** Retrofitted with vertical CFRP2 bars. **b** Retrofitted with vertical SGFRP bars

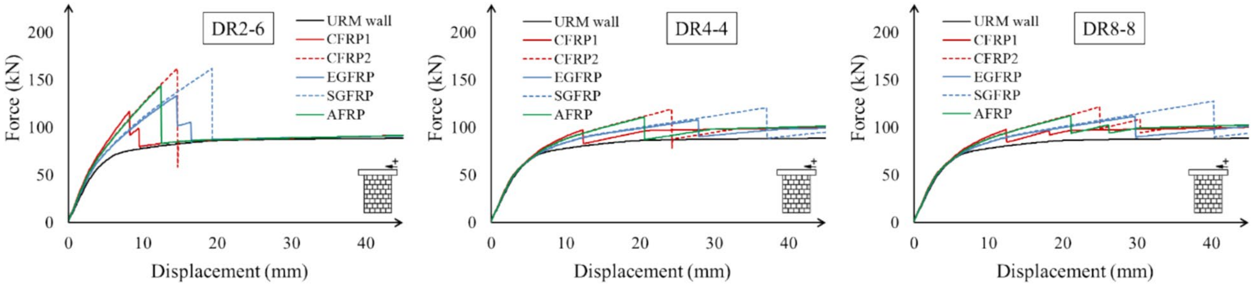

Fig. 7 The load–displacement curve of walls retrofitted with diagonal FRP bars ($\sigma = 1.25$ MPa)

low vertical loads ($\sigma = 0.2$ and 0.5 MPa), the DR8-8 model with SGFRP maintained the target displacement before failure, although it ultimately failed before reaching the target displacement. Thus, the combination of SGFRP with the DR8-8 configuration can be viewed as the most effective diagonal option.

To determine the optimal configuration based on bar materials and layout, load–displacement curves for vertical and diagonal setups were compared. Vertical configurations offer greater overstrength and hardening stiffness compared to diagonal setups. As a result, the VR7-6/SGFRP combination is identified as the most effective case for retrofitting dry-stack masonry walls. Because SGFRP did not fail at the target displacement, it can offer significant stiffness during cyclic loading.

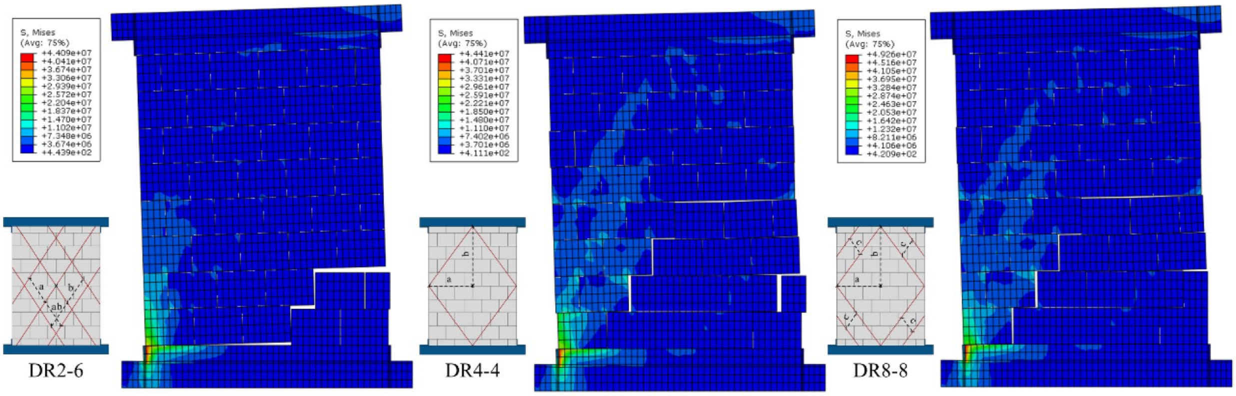

(a) Retrofitted with diagonal CFRP2 bars

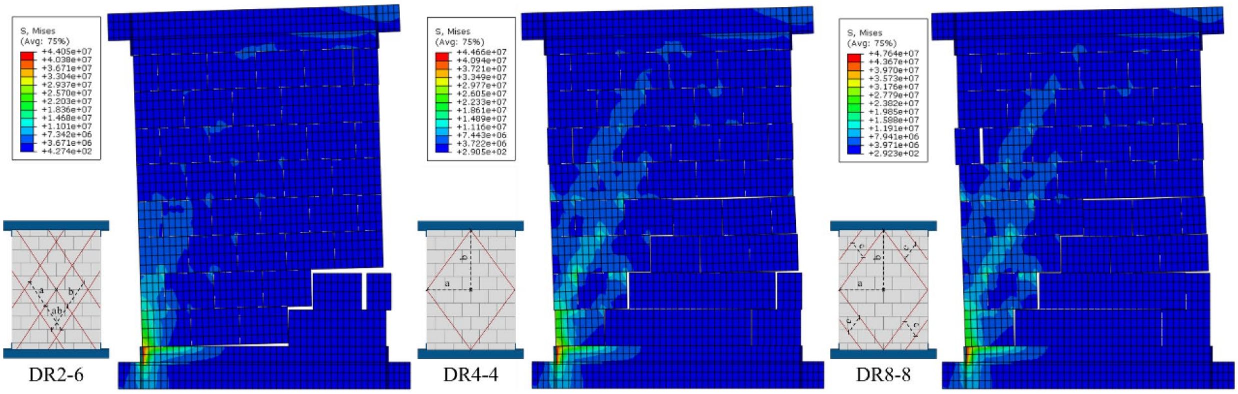

(b) Retrofitted with diagonal SGFRP bars

Fig. 8 The failure mechanism of walls retrofitted with diagonal CFRP2 and SGFRP bars ($\sigma = 1.25$ MPa). **a** Retrofitted with diagonal CFRP2 bars. **b** Retrofitted with diagonal SGFRP bars

4.3 Cyclic Analysis

As previously mentioned, the VR7-6 model with vertical bars and the DR8-8 model with diagonal bars demonstrated the best performance. The analysis revealed that VR7-6 offers significantly greater overstrength and hardening stiffness compared to DR8-8. This comparison is grounded in the results from the pushover analysis. For a more thorough comparison, the cyclic analyses of VR7-6 and DR8-8 using the most efficient materials are discussed in this section. The cyclic analysis was conducted using the loading protocol shown in Fig. 10 (Vasconcelos, 2005).

Fig. 11 illustrates the hysteresis loops for both original and retrofitted walls in the VR7-6 and DR8-8 models under upper and lower vertical loads. A key observation across all cases is that hysteresis loops became more stable as vertical loads increased, particularly for the VR7-6 model. Additionally, the DR8-8 model exhibited considerably narrower hysteresis loops than VR7-6, regardless of material, which can be viewed as a notable drawback for DR8-8 when compared to VR7-6. The behavior of retrofitted walls with either stainless steel or titanium was quite comparable.

For the VR7-6 model with stainless steel or titanium bars, the cycles exhibited near symmetry under lower vertical loads. A biased loop shape, similar to that of the original wall, was observed at higher vertical loads, with the overall hysteresis performance closely matching that of the original walls. Nonetheless, there was an improvement in free sliding during unloading. In contrast, observations of the DR8-8 model with stainless steel or titanium bars revealed notable differences. First, the hysteresis loops remained symmetrical under all levels of vertical load, but no improvement in free sliding during unloading was observed. For models incorporating CFRP2 and SGFRP (whether VR7-6 or DR8-8), the bias in hysteresis loops was much lower compared to models with stainless steel and titanium bars, since FRP materials predominantly remained in the elastic range before failure. Also, free sliding at the unloading stage was similar to that observed during pushover analysis for VR7-6 and DR8-8 models. The cyclic analysis results revealed that

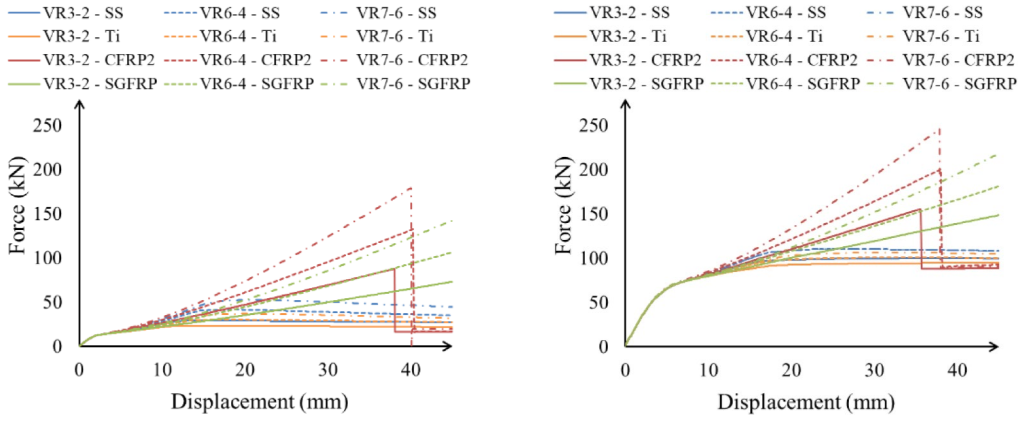

(a) Vertical, $\sigma = 0.2$ MPa (b) Vertical, $\sigma = 1.25$ MPa

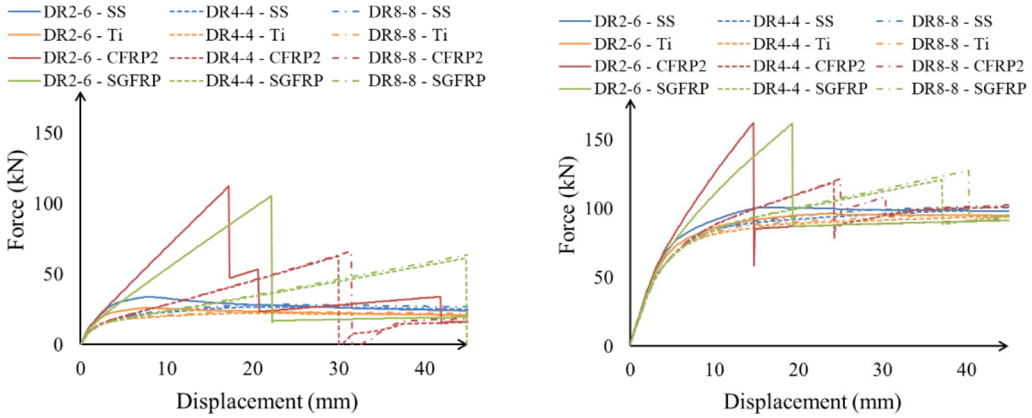

(c) Diagonal, $\sigma = 0.2$ MPa (d) Diagonal, $\sigma = 1.25$ MPa

Fig. 9 Comparison of material properties for vertical and diagonal arrangements under lower and upper levels of vertical load (σ)

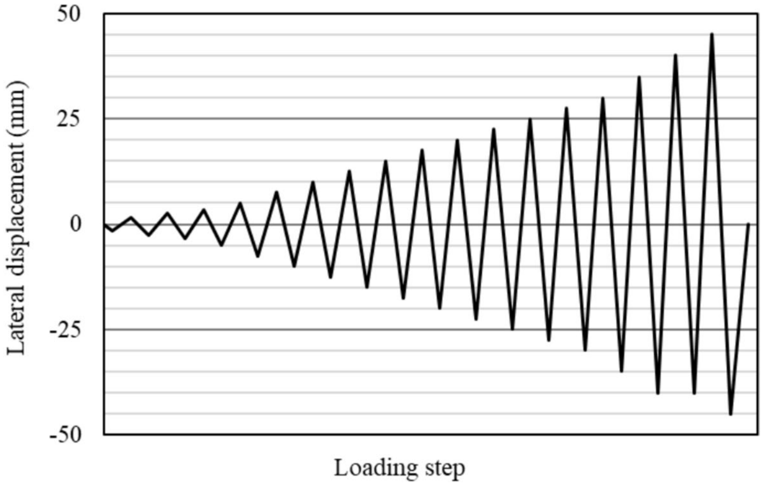

Fig. 10 Cyclic loading protocol

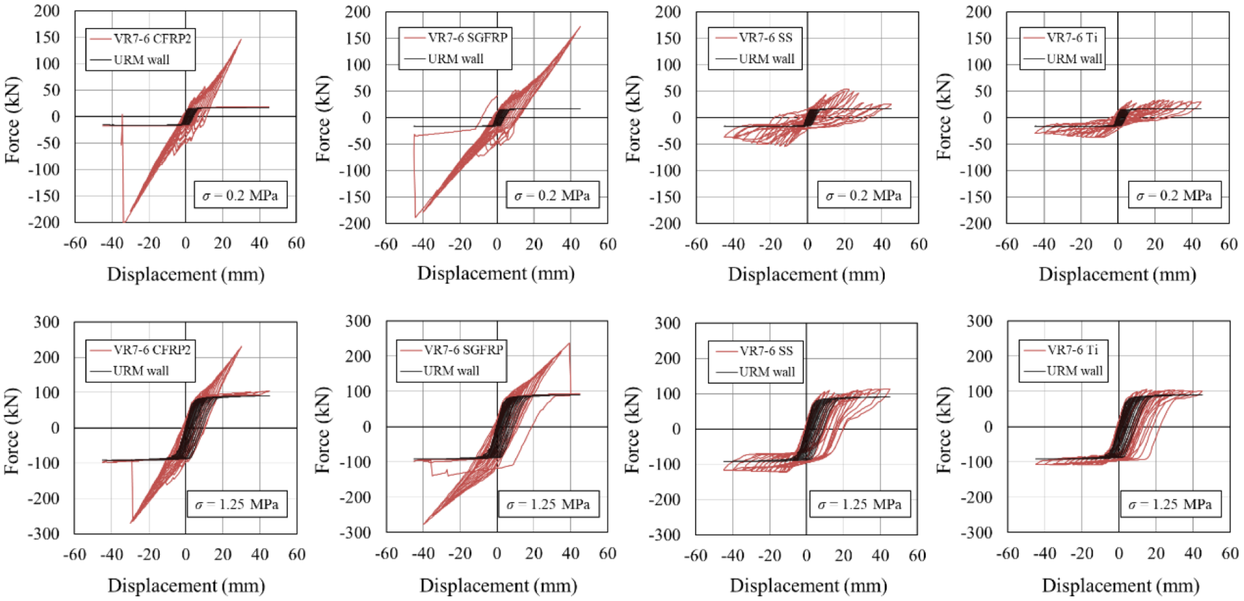

(a) Vertical arrangement – VR7-6 model

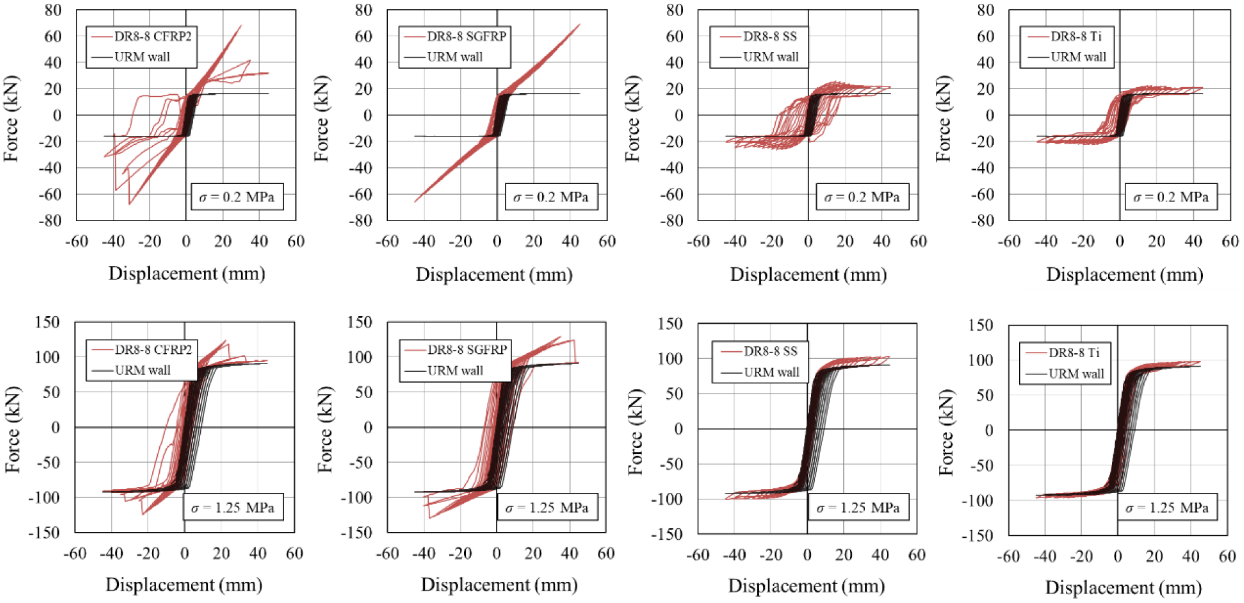

(b) Diagonal arrangement – DR8-8 model

Fig. 11 Cyclic behavior of the most optimized models under lower and upper levels of vertical load (σ) for vertical and diagonal arrangements

CFRP2 bars greatly enhanced wall strength and hardening stiffness, though they failed at smaller deformations than the target displacement. Although SGFRP bars in the DR8-8 model did not fail under low vertical loads, they experienced failure at higher vertical loads. The VR7-6 model with SGFRP failed during the final cycle at a target displacement of 45 mm, except at $\sigma = 1.25$ MPa, where failure occurred one cycle earlier at a displacement of 40 mm.

It is important to mention that during both the pushover and cyclic analyses, the load was applied through displacement control and gradually increased. As a result, any shock that may occur in the system during FRP failure is not captured. Addressing this issue will requires further research, specifically by examining wall behavior under seismic loads, potentially through dynamic analysis, which falls outside the scope of this study. Of all the models, the VR7-6/SGFRP configuration demonstrated the best overall performance. In most cases, the bars failed at the target displacement. The wall's behavior was enhanced through the addition of considerable overstrength and hardening stiffness to the system, as demonstrated by the pushover analysis. Moreover, it significantly improved hysteresis behavior by reducing loop bias and limiting free sliding, which increased the hysteresis area, thereby absorbing more energy.

Table 6 presents the normalized dissipated energy of the models in comparison to the URM wall results. In every case, increasing the vertical load led to a reduction in normalized dissipated energy. The VR7-6 model displayed significantly higher values than DR8-8, further demonstrating its superiority. In the DR8-8 model, CFRP2 exhibited higher values than SGFRP at lower vertical loads but lower values at higher vertical loads. However, CFRP2 bars failed at smaller lateral displacement compared to SGFRP, diminishing its efficiency. In the VR7-6 model, SGFRP had higher values than CFRP2 across all vertical loads. Titanium and stainless steel also delivered comparable dissipated energy levels to SGFRP, particularly at higher vertical loads. However, SGFRP proved to be more effective due to its ability to provide substantial hardening stiffness and overstrength.

Table 6 Normalized value of cyclic dissipated energy of retrofitted walls

Type	Material	Vertical load (MPa)			
		$\sigma=0.2$	$\sigma=0.5$	$\sigma=0.875$	$\sigma=1.25$
VR7-6	Ti	35.86	10.53	8.57	4.49
	SS	40.86	15.71	10.60	7.51
	CFRP2	52.94	17.23	10.25	6.88
	SGFRP	77.59	26.39	16.19	8.91
DR8-8	Ti	24.62	4.78	2.27	1.53
	SS	36.04	9.10	3.62	2.08
	CFRP2	28.79	12.41	5.73	3.75
	SGFRP	17.92	11.66	5.73	5.37

5 Conclusions

To improve the seismic performance of dry-stack masonry walls while maintaining the visual integrity of the structure, embedded bars were suggested. The effectiveness of the retrofit method was assessed using various materials, including stainless steel, titanium, and common FRP types, with different bar arrangements (horizontal, vertical, and diagonal). The results indicated that horizontal bar arrangements were ineffective in enhancing the mechanical behavior of the wall. In contrast, vertical and diagonal arrangements significantly improved wall performance in terms of overstrength and hardening stiffness. Vertical bars proved more effective than diagonal bars in enhancing overstrength, hardening stiffness, and ductility (in the case of FRP materials). The findings indicate that the VR7-6 configuration was the most efficient. Furthermore, FRP materials demonstrated greater overstrength and hardening stiffness compared to stainless steel and titanium bars. However, due to the brittle nature of FRP, bars frequently broke before reaching the target displacement, making them more sensitive to the arrangement. Conversely, stainless steel and titanium exhibited significant lateral deformation due to their plastic behavior. Among FRP materials, CFRP2 demonstrated the highest levels of overstrength and hardening stiffness. SGFRP, on the other hand, maintained the target displacement without failure and showed a similar level of overstrength to CFRP2. For vertical bars, SGFRP did not fail under the target displacement across at any of the four tested levels of vertical load. However, under high vertical load, it failed in diagonal arrangements, reducing its efficiency. When used in the VR7-6 configuration, SGFRP offered a substantial overstrength ratio (0.81 at $\sigma=0.2$ MPa and 2.44 at $\sigma=1.25$ MPa) and hardening stiffness ratio (0.44 at $\sigma=0.2$ MPa and 0.32 at $\sigma=1.25$ MPa). Moreover, it could sustain considerable lateral deformation, making it the most efficient material in this setup. A set of cyclic analyses was performed for further investigation. These analyses also confirmed that VR7-6 model with SGFRP bars has the best performance among the proposed models. The hysteresis loops remained stable and improved as the vertical load increased. Because SGFRP bars in the VR7-6 model remained within the elastic range, except during the final cycles, two key defects observed in the original wall's hysteresis loops, bias and free sliding at the start of unloading, were nearly eliminated. Once stiffness was recovered, the loops expanded, and the energy absorbed by the wall increased significantly. The amount of energy dissipation ratio of the model and base wall was 77.59 ($\sigma=0.2$ MPa) or 8.91 ($\sigma=1.25$ MPa), which is a notable value. In cases where SGFRP bars are not feasible due to cost or availability, stainless steel and titanium bars can be considered better alternatives to other FRP materials. While stainless steel and titanium bars did not enhance overstrength and hardening stiffness as much as certain FRP materials (like CFRP2), they did offer ductile behavior. Other FRPs exhibited limited lateral deformation capacity, a key factor in achieving desirable seismic performance. It should be noted that, in real projects, the optimum case may need to be decided in accordance with cost considerations. Given the variation in construction and material costs worldwide, one material may be a better option than the others in a specific region. When considering cost as a function of the materials used, the optimal layout, which minimizes material while achieving the desired behavior, will inherently have the lowest cost. It is important to recognize that real-world masonry construction may deviate from the idealizations utilized in numerical models. In practice, variations in construction quality, including masonry workmanship, may impact the performance of retrofitting strategies. In case of significant deviation between construction and idealization in this study, the conclusion of this study may need to be interpreted cautiously and adjusted accordingly to account for these practical limitations.

Acknowledgements
The authors would like to acknowledge Seoul National University of Science and Technology for the support to this study.

Author contributions
FY made substantial contributions to the conception and design of the work, the acquisition, analysis, and interpretation of data, and drafted the work. CK made contributions to the conception and design of the work, the interpretation of data, and substantively revised the work. TK made contributions to the conception and design of the work, the interpretation of data, and substantively revised the work. All authors read and approved the final manuscript.

Funding
This study was financially supported by Seoul National University of Science and Technology.

Availability of data and materials
All data generated or analyzed during this study are included in this published article.

Declarations

Competing interests
The authors declare that they have no competing interests.

Received: 30 September 2024 Accepted: 7 April 2025

References

Abaqus (2020). ABAQUS documentation. Dassault Systèmes Simulia Corporation, Providence, RI. https://www.3ds.com/support/documentation/user-guides

Abdulsalam, B., Ali, A. H., ElSafty, A., & Elshafey, N. (2021). Behavior of GFRP strengthening masonry walls using glass fiber composite anchors. *Structures, 29*, 1352–1361. https://doi.org/10.1016/j.istruc.2020.12.025

Afzali, S., Alinejad, H., Nasrollahzadeh, K., & Kang, T.H.-K. (2021). Modeling of near-surface-mounted fiber-reinforced polymer strips to concrete. *ACI Structural Journal*. https://doi.org/10.14359/51732866

Askar, M. K., Hassan, A. F., & Al-Kamaki, Y. S. (2022). Flexural and shear strengthening of reinforced concrete beams using FRP composites: A state of the art. *Case Studies in Construction Materials*. https://doi.org/10.1016/j.cscm.2022.e01189

Bhattacharya, S., Nayak, S., & Dutta, S. C. (2014). A critical review of retrofitting methods for unreinforced masonry structures. *International Journal of Disaster Risk Reduction, 7*, 51–67. https://doi.org/10.1016/j.ijdrr.2013.12.004

Bui, T. L., Larbi, A. S., Reboul, N., & Ferrier, E. (2015). Shear behaviour of masonry walls strengthened by external bonded FRP and TRC. *Composite Structures, 132*, 923–932. https://doi.org/10.1016/j.compstruct.2015.06.057

Capozucca, R. (2011). Experimental analysis of historic masonry walls reinforced by CFRP under in-plane cyclic loading. *Composite Structures, 94*(1), 277–289. https://doi.org/10.1016/j.compstruct.2011.06.007

ElGawady, M., Lestuzzi, P., and Badoux, M. (2004). A review of retrofitting of unreinforced masonry walls using composites. *In Proceedings of 4th International conference on advanced composite materials in bridges and structures*. CSCE, Calgary, Alberta, Canada. https://www.researchgate.net/publication/37447218_A_Review_of_Retrofitting_of_URM_Walls_Using_Composites

Galati, N., Nanni, A., Dharanib, L., Focacci, F., & Aiello, M. A. (2006). Thermal effects on bond between FRP rebars and concrete. *Composites Part a: Applied Science and Manufacturing., 37*(6), 1223–1230. https://doi.org/10.1016/j.compositesa.2005.05.043

Gentry, T. R., & Hudak, C. E. (1996). Thermal compatibility of plastic composite reinforcement and concrete. *Advanced Composite Materials in Bridges and Structures*. https://doi.org/10.1061/(ASCE)1090-0268(1999)3:2(82)

Golden, L. B., Lane, I. R., & Acherman, W. L. (1952). Corrosion resistance of titanium, zirconium, and stainless steel. *Industrial & Engineering Chemistry, 44*(8), 1930–1939. https://doi.org/10.1021/ie50512a050

Huang, B., & Lu, W. (2021). Experimental investigation of the uniaxial compressive behavior of thin building granite. *Construction and Building Materials, 267*, 120967. https://doi.org/10.1016/j.conbuildmat.2020.120967

Islam, R. (2008). *Inventory of FRP strengthening methods in masonry structures*. Master thesis, Universitat Politècnica de Catalunya, Barcelona, Spain. http://hdl.handle.net/2099.1/7901

Jafari, A., Oskouei, A. V., Bazli, M., & Ghahri, R. (2018). Effect of the FRP sheet's arrays and NSM FRP bars on in-plane behavior of URM walls. *Journal of Building Engineering, 20*, 679–695. https://doi.org/10.1016/j.jobe.2018.09.018

Jing, J., Zhou, C., Zhang, C., & Li, T. (2023). In-plane cyclic behavior of brick walls strengthened with CFRP plates embedded in the horizontal mortar joint. *Journal of Building Engineering, 63*, 105476. https://doi.org/10.1016/j.jobe.2022.105476

Ludovico-Marques, M., Chastre, C., & Vasconcelos, G. (2012). Modelling the compressive mechanical behaviour of granite and sandstone historical building stones. *Construction and Building Materials, 28*(1), 372–381. https://doi.org/10.1016/j.conbuildmat.2011.08.083

Noor-E-Khuda, S., Dhanasekar, M., & Thambiratnam, D. P. (2016). Out-of-plane deformation and failure of masonry walls with various forms of reinforcement. *Composite Structures, 140*, 262–277. https://doi.org/10.1016/j.compstruct.2015.12.028

Paganoni, S., and D'Ayala, D. (2015). *Dissipative anchor devices for the seismic retrofit of heritage buildings*. Doctoral Dissertation, University of Bath, England. https://purehost.bath.ac.uk/ws/portalfiles/portal/187963831/Dissipative_Anchor_Devices_final.pdf

Saghafi, M. H., Safakhah, S., Kheyroddin, A., & Mohammadi, M. (2014). In-plane shear behavior of FRP strengthened masonry walls. *APCBEE Procedia, 9*, 264–268. https://doi.org/10.1016/j.apcbee.2014.01.047

Sayin, B., Yildizlar, B., Akcay, C., & Gunes, B. (2019). The retrofitting of historical masonry buildings with insufficient seismic resistance using conventional and non-conventional techniques. *Engineering Failure Analysis, 97*, 454–463. https://doi.org/10.1016/j.engfailanal.2019.01.031

Shrestha, K. C., Nagae, T., & Araki, Y. (2011). Finite element study on pinning retrofitting technique of masonry walls with opening subjected to in-plane shear load. *ACEE Journal, 4*(4), 81–96.

Shrestha, K. C., Nagae, T., & Araki, Y. (2011b). Finite element modeling of cyclic out-of-plane response of masonry walls retrofitted by inserting inclined stainless steel bars. *Journal of Disaster Research, 6*(1), 36–43. https://doi.org/10.20965/jdr.2011.p0036

Soleymani, A., Najafgholipour, M. A., Johari, A., & Jowkar, S. (2023). In-plane shear strengthening of traditional unreinforced masonry walls with near surface mounted GFRP bars. *Construction and Building Materials, 367*, 130362. https://doi.org/10.1016/j.conbuildmat.2023.130362

Torres, N., Tumialan, J. G., Nanni, A., Bennet, R. M., & Basalo, F. J. D. C. (2022). Flexural design of masonry walls reinforced with FRP bars based on full-scale structural tests. *Special Publication., 356*, 291–311. https://doi.org/10.14359/51737277

Turco, V., Secondin, S., Morbin, A., Valluzzi, M. R., & Modena, C. (2006). Flexural and shear strengthening of un-reinforced masonry with FRP bars.

Composites Science and Technology, 66(2), 289–296. https://doi.org/10.1016/j.compscitech.2005.04.042

Vasconcelos, G. (2005). *Experimental investigations on the mechanics of stone masonry: characterization of granites and behavior of ancient masonry shear walls*. Doctoral Dissertation, University of Minho, Portugal. https://hdl.handle.net/1822/17383

Vasconcelos, G., Lourenço, P. B., Alves, C. A. S., & Pamplona, J. (2009). Compressive behavior of granite: Experimental approach. *ASCE Journal of Materials in Civil Engineering, 21*(9), 502–511. https://doi.org/10.1061/(ASCE)0899-1561(2009)21:9(502)

Vintzileou, E., and Papadopoulos, K. (2001). Dowel action of titanium bars connecting marble elements. *In Proceedings of international RILEM symposium on connections between steel and concrete*. https://www.rilem.net/publication/publication/26?id_papier=1903

Wang, C., Sarhosis, V., & Nikitas, N. (2018). Strengthening/retrofitting techniques on unreinforced masonry structure/element subjected to seismic loads: A literature review. *The Open Construction and Building Technology Journal*. https://doi.org/10.2174/1874836801812010251

Yavartanoo, F., & Kang, T.H.-K. (2022). Dry-Stack masonry wall modeling using finite element method. *ASCE Journal of Structural Engineering, 148*(11), 04022176. https://doi.org/10.1061/(ASCE)ST.1943-541X.0003457

Yavartanoo, F., & Kang, T.H.-K. (2022a). Retrofitting of unreinforced masonry structures and considerations for heritage-sensitive constructions. *Journal of Building Engineering*. https://doi.org/10.1016/j.jobe.2022.103993

Yavartanoo, F., Kang, T.H.-K., Ha, T. U., Lim, W. Y., & Hong, S. G. (2020). Restoration of Mireuksaji stone pagoda: Evaluation of reinforced granite members with titanium bars. *ASCE Journal of Performance of Constructed Facilities, 34*(4), 04020046. https://doi.org/10.1061/(ASCE)CF.1943-5509.0001454

Yavartanoo, F., Kang, T.H.-K., Jeon, S., & Hong, S. G. (2019). Investigation of material and structural performance of Mireuksaji stone pagoda. *ASCE Journal of Performance of Constructed Facilities, 33*(6), 04019059. https://doi.org/10.1061/(ASCE)CF.1943-5509.0001326

Zamani Ahari, G. (2013). *Structural in-plane behavior of masonry walls externally retrofitted with fiber reinforced materials*. Doctoral Dissertation, Kyushu University, Fukuoka, Japan. https://api.lib.kyushu-u.ac.jp/opac_download_md/1398305/hues0303.pdf

Publisher's Note

Fahimeh Yavartanoo is a post-doctoral researcher at Seoul National University of Science and Technology in Korea.

Chang-Soo Kim is a professor at Seoul National University of Science and Technology in Korea.

Thomas H.-K. Kang is a professor at Seoul National University in Korea.